

Temperature-Stable Tunneling Current in Serial Double Quantum Dots: Insights from Nonequilibrium Green Functions and Pauli Spin Blockade

David M T Kuo

*Department of Electrical Engineering and Department of Physics,
National Central University, Chungli, 32001 Taiwan, China*

(Dated: January 28, 2025)

We theoretically investigate charge transport through serial double quantum dots (SDQDs) with strong electron correlations using nonequilibrium Green's function techniques. In the linear response regime, we compute the charge stability diagram and analyze the Coulomb oscillatory tunneling current, revealing both thermal and nonthermal broadening effects on the current spectra in relation to two gate voltages. In the nonlinear response regime, we focus on tunneling currents in SDQDs under the Pauli spin blockade (PSB) scenario. We find that current rectification with negative differential conductance is significantly degraded as temperature increases, making it challenging to distinguish between the inter-site spin triplet and singlet states. Notably, we observe a robust reversed tunneling current that remains stable against temperature variations, provided the resonant channel in the PSB scenario is coupled to the states of the right (left) electrode, which is fully occupied (unoccupied) by particles. This characteristic provides valuable insights for designing transistors capable of operating over a wide temperature range.

I. INTRODUCTION

Impurities play a crucial role in influencing electron transport in metals[1-6], as evidenced by phenomena such as Anderson localization[1-3] and the Kondo effect[4-6]. These effects highlight the complex interactions that occur in systems with impurities, necessitating advanced engineering techniques to achieve precise control over electron transport at the level of single atomic impurities. Notably, the resonant electrical conductance peak exhibits distinctive temperature behavior, which varies based on whether the temperature is below or above the Kondo temperature. Expanding on the study of single impurities, researchers are now investigating charge transport through serial double quantum dots (SDQDs)[7-8], which are often referred to as artificial atoms. This area of research has uncovered fascinating phenomena, including single-electron coherent tunneling between quantum dots[7-9] and current rectification due to two-electron triplet state blockade [10-17]. Furthermore, SDQDs hold significant promise for applications in devices such as quantum bits[18], quantum current sensors [19], and spintronics [20,21]. However, a critical challenge remains in ensuring reproducibility during the implementation of SDQD devices.

Graphene nanoribbons (GNRs) present unique advantages due to the topological states that emerge in the middle of their subband structures. These states are well-isolated from both the conduction and valence bands, allowing their wave functions to be less susceptible to noise from other excited modes[22-26]. The bottom-up synthesis technique provides precise control over GNR segments and their heterojunctions at the atomic level. This level of precision facilitates the formation of SDQDs without the typical issues associated with size fluctuations and uncertainties in separation distances[25]. Moreover, the Coulomb interactions, electron hopping strengths, and tunneling rates within these topological states can be en-

gineered to meet specific requirements. When compared to double quantum dots constructed from traditional materials like silicon, germanium, and gallium arsenide[9-17], the reproducibility of GNR heterojunctions positions them as promising building blocks for future quantum circuits[27].

Despite significant theoretical advancements in understanding charge transport through SDQDs within the Coulomb blockade regime[28-37], deriving a comprehensive formula for tunneling current that accounts for all experimentally observed phenomena remains a challenge[7-17]. This study presents an analytical expression for the transmission coefficient that effectively describes the transport properties of SDQDs, specifically those formed by the topological states of 9-7-9 armchair graphene nanoribbons (AGNRs) in the absence of spin-orbit interactions and external magnetic fields[23] (see Figure. 1). Our research focuses on elucidating the temperature dependence of tunneling current in the Pauli spin blockade (PSB) configuration. Notably, we find that nonthermal broadening results in reversed tunneling currents that remain robust across a wide temperature range. Transistors exhibiting these characteristics can make them crucial components in circuits for artificial intelligence applications or in extreme temperature environments, **such as** space exploration, high-temperature industrial applications, and scientific instruments used in harsh conditions.

II. CALCULATION METHODOLOGY

To investigate charge transport through SDQDs formed by AGNR heterojunctions [23,26] in the absence of spin-orbit interaction and magnetic fields, we utilize a two-site Hubbard model. The Hamiltonian of this model, coupled to the electrodes, is expressed as $H = H_0 + H_{2-site}$, where

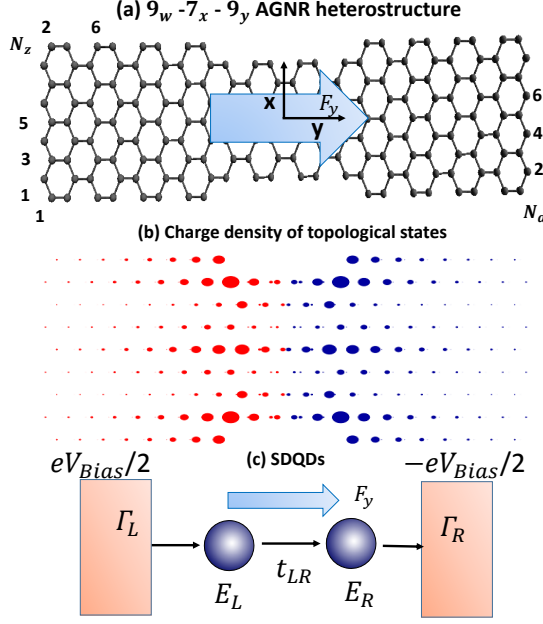


FIG. 1: (a) Schematic diagram of a finite $9_w - 7_x - 9_y$ armchair graphene nanoribbon (AGNR) structure subjected to a uniform electric field (F_y). The y-direction is defined along the armchair edge structure of $9_w - 7_x - 9_y$ AGNR structure. The subscripts w, x, and y in the notation $9_w - 7_x - 9_y$ denote the segment lengths of the AGNR heterostructures in terms of the unit cell (u.c.). (b) Charge density distribution of the topological states in the $9_w - 7_x - 9_y$ AGNR structure at $F_y = 0$. The radius of each circle represents the magnitude of the charge density for the topological states. The red and blue colors correspond to the topological states originating from the left and right interface states of the $9_w - 7_x - 9_y$ AGNR structure, respectively. (c) Charge transport through the interface states of a $9-7-9$ AGNR with zigzag edges, coupled to electrodes, modeled as a serial double quantum dot system (SDQDs). The symbols Γ_L and Γ_R denote the electron tunneling rates between the left and right electrodes.

$$\begin{aligned}
 H_0 = & \sum_{k,\sigma} \epsilon_k a_{k,\sigma}^\dagger a_{k,\sigma} + \sum_{k,\sigma} \epsilon_k b_{k,\sigma}^\dagger b_{k,\sigma} \\
 & + \sum_{k,\sigma} V_{k,L} d_{L,\sigma}^\dagger a_{k,\sigma} + \sum_{k,\sigma} V_{k,R} d_{R,\sigma}^\dagger b_{k,\sigma} + h.c.
 \end{aligned} \quad (1)$$

The first two terms of Eq. (1) describe the free electrons in the left and right electrodes. $a_{k,\sigma}^\dagger$ ($b_{k,\sigma}^\dagger$) creates an electron of momentum k and spin σ with energy ϵ_k in the left (right) electrode. $V_{k,L}$ ($V_{k,R}$) describes the coupling between the left (right) lead and the left (right) site.

$$\begin{aligned}
 H_{2-site} = & \sum_{j,\sigma} E_j c_{j,\sigma}^\dagger c_{j,\sigma} - t_{LR} (c_{R,\sigma}^\dagger c_{L,\sigma} + c_{L,\sigma}^\dagger c_{R,\sigma}) \\
 & + \sum_j U_j n_{j,\sigma} n_{j,-\sigma} + \frac{1}{2} \sum_{j \neq \ell, \sigma, \sigma'} U_{j,\ell} n_{j,\sigma} n_{\ell,\sigma'},
 \end{aligned} \quad (2)$$

where E_j represents the spin-independent energy level of the localized state, $U_j = U_{L(R)} = U_0$ and $U_{j,\ell} = U_{LR} = U_1$ denote the intra-site and inter-site Coulomb interactions, respectively. In this study, we adopt $U_0 = 150$ meV and $U_1 = 40$ meV for the interface states of the $9_w - 7_x - 9_y$ AGNR heterojunction, where w , x and y , with units in terms of the unit cell of AGNRs [38].

Using the equations of motion for the retarded and lesser Green's functions [39,40], we derive a closed-form expression for the tunneling current flowing from the left (right) electrode, expressed as:

$$\begin{aligned}
 J_{L(R)}(V_{bias}, T) = & \frac{2e}{h} \int d\varepsilon \mathcal{T}_{LR(RL)}(\varepsilon) [f_L(\varepsilon) - f_R(\varepsilon)].
 \end{aligned} \quad (3)$$

The Fermi distribution function for the α -th electrode is defined as $f_\alpha(\varepsilon) = 1/(\exp[(\varepsilon - \mu_\alpha)/k_B T] + 1)$, where $\mu_{L(R)} = E_F \pm eV_{bias}/2$ is the chemical potential of the left (right) electrode with an applied bias of $V_{bias}/2$ and $-V_{bias}/2$, respectively. The transmission coefficient $\mathcal{T}_{LR}(\varepsilon)$ is expressed analytically as:

$$\begin{aligned}
 \mathcal{T}_{LR}(\varepsilon)/(4t_{LR}^2 \Gamma_L \Gamma_R) = & \frac{C_1}{|\epsilon_L \epsilon_R - t_{LR}^2|^2} \\
 & + \frac{C_2}{|(\epsilon_L - U_{LR})(\epsilon_R - U_R) - t_{LR}^2|^2} \\
 & + \frac{C_3}{|(\epsilon_L - U_{LR})(\epsilon_R - U_{LR}) - t_{LR}^2|^2} \\
 & + \frac{C_4}{|(\epsilon_L - 2U_{LR})(\epsilon_R - U_{LR} - U_R) - t_{LR}^2|^2} \\
 & + \frac{C_5}{|(\epsilon_L - U_L)(\epsilon_R - U_{LR}) - t_{LR}^2|^2} \\
 & + \frac{C_6}{|(\epsilon_L - U_L - U_{LR})(\epsilon_R - U_R - U_{LR}) - t_{LR}^2|^2} \\
 & + \frac{C_7}{|(\epsilon_L - U_L - U_{LR})(\epsilon_R - 2U_{LR}) - t_{LR}^2|^2} \\
 & + \frac{C_8}{|(\epsilon_L - U_L - 2U_{LR})(\epsilon_R - U_R - 2U_{LR}) - t_{LR}^2|^2},
 \end{aligned} \quad (4)$$

where $\epsilon_L = \varepsilon - E_L + i\Gamma_L$ and $\epsilon_R = \varepsilon - E_R + i\Gamma_R$. The tunneling rate $\Gamma_{L(R)}(\varepsilon) = 2\pi \sum_{k,\sigma} |V_{k,L(R)}|^2 \delta(\varepsilon - \epsilon_k)$ arises from the QD coupled to electrode. The transmission coefficient in Eq.(4) encompasses eight terms, each corresponding to one of the eight possible configurations of the SDQD that a particle with spin σ from the left electrode may encounter: (a) both sites empty, (b) one particle with spin $-\sigma$ on the right site, (c) one particle

with spin σ on the right site, (d) two particles on the right-site, (e) one particle with spin $-\sigma$ on the left-site, (f) both sites filled by one particle with spin $-\sigma$, (g) one particle with spin $-\sigma$ on the left site and one particle with spin σ on the right site and (h) one particle with spin $-\sigma$ on the left site and two particle on the right-site. The probabilities of these configurations are expressed as follow:

$$\begin{aligned}
C_1 &= 1 - N_{L,\sigma} - N_{R,\sigma} - N_{R,-\sigma} + \langle n_{R,\sigma} n_{L,\sigma} \rangle \\
&\quad + \langle n_{R,-\sigma} n_{L,\sigma} \rangle + \langle n_{R,-\sigma} n_{R,\sigma} \rangle - \langle n_{R,-\sigma} n_{R,\sigma} n_{L,\sigma} \rangle \\
C_2 &= N_{R,\sigma} - \langle n_{R,\sigma} n_{L,\sigma} \rangle - \langle n_{R,-\sigma} n_{R,\sigma} \rangle \\
&\quad + \langle n_{R,-\sigma} n_{R,\sigma} n_{L,\sigma} \rangle \\
C_3 &= N_{R,-\sigma} - \langle n_{R,-\sigma} n_{L,\sigma} \rangle - \langle n_{R,-\sigma} n_{R,\sigma} \rangle \\
&\quad + \langle n_{R,-\sigma} n_{R,\sigma} n_{L,\sigma} \rangle \\
C_4 &= \langle n_{R,-\sigma} n_{R,\sigma} \rangle - \langle n_{R,-\sigma} n_{R,\sigma} n_{L,\sigma} \rangle \\
C_5 &= N_{L,\sigma} - \langle n_{R,\sigma} n_{L,\sigma} \rangle - \langle n_{R,-\sigma} n_{L,\sigma} \rangle \\
&\quad + \langle n_{R,-\sigma} n_{R,\sigma} n_{L,\sigma} \rangle \\
C_6 &= \langle n_{R,\sigma} n_{L,\sigma} \rangle - \langle n_{R,-\sigma} n_{R,\sigma} n_{L,\sigma} \rangle \\
C_7 &= \langle n_{R,-\sigma} n_{L,\sigma} \rangle - \langle n_{R,-\sigma} n_{R,\sigma} n_{L,\sigma} \rangle \\
C_8 &= \langle n_{R,-\sigma} n_{R,\sigma} n_{L,\sigma} \rangle,
\end{aligned}$$

where $N_{\ell,\sigma}$ is the single particle occupation number with spin σ at site ℓ . The intra-site and inter-site two-particle correlation functions are denoted by $\langle n_{\ell,-\sigma} n_{\ell,\sigma} \rangle$ and $\langle n_{\ell,\sigma} n_{j,\sigma} \rangle$ ($\langle n_{\ell,-\sigma} n_{j,\sigma} \rangle$), respectively. The three-particle correlation function is represented by $\langle n_{\ell,-\sigma} n_{\ell,\sigma} n_{j,\sigma} \rangle$. These correlation functions can be solved self-consistently (see Appendix A), ensuring that probability conservation is maintained, as indicated by $\sum_m C_m = 1$. To obtain the reversed bias tunneling current, we can simply exchange the indices of $\mathcal{T}_{LR}(\varepsilon)$ in Eq. (4).

III. RESULTS AND DISCUSSION

A. Tunneling Current at Small Applied Bias

To reflect the experimental conditions, we set the energies $E_L = -(\delta_1 e V_{g,L} + (1 - \delta_1) e V_{g,R}) + \eta e V_{Bias}$ and $E_R = -((1 - \delta_2) e V_{g,L} + \delta_2 e V_{g,R}) - \eta e V_{Bias}$, where δ_1 and δ_2 are determined by the inter-site and intra-site electron Coulomb interactions[33]. The parameter $\eta < 1/2$ serves to adjust the orbital offset induced by the applied bias V_{Bias} . $V_{g,L}$ and $V_{g,R}$ are the left and right gate voltages, respectively. In Fig. 2, we present the calculated charge stability diagrams and tunneling currents as functions of the two gate voltages for small applied biases (V_{Bias}), aiming to replicate earlier experimental and theoretical findings [33,34], where the authors considered the case of $\Gamma_{L(R)} = \Gamma_t = 0$ and $T = 0$.

As shown in Fig. 2(a), nine regions (plateaus) are marked by integer values (N_L, N_R) , where $N_L = \sum_{\sigma} N_{L,\sigma}$ and $N_R = \sum_{\sigma} N_{R,\sigma}$ represent the charge numbers of the left and right sites, respectively. The total

charge number across the two sites is given by $N_t = \sum_{\sigma} (N_{L,\sigma} + N_{R,\sigma})$. Since $N_{L(R)}$ is a statistical average, N_L and N_R can take fractional values in the transition areas of N_t , reflecting the characteristics of an open system. The shapes of the regions corresponding to (N_L, N_R) in the charge stability diagram (Fig. 2(a)) are consistent with the results from Ref. [34], attributable to the conditions $k_B T \ll U_0$ and $t_{LR} \leq \Gamma_t$. The charge stability diagram of $t_{LR} > \Gamma_t$ is illustrated in Appendix B. Charge transport through graphene SDQD under the condition of $t_{LR} > \Gamma_t$ (coherent tunneling) have been experimentally studied[41-45]. Our current study is limited to the case where $t_{LR} \leq \Gamma_t$.

Observable quantities, such as the spectra of electrical conductance, provide deeper insights into the intricate structures of SDQD devices, particularly regarding their contact properties with electrodes. In Fig. 2(b), we present the tunneling current corresponding to the charge stability diagram shown in Fig. 2(a). When $V_{g,L} = V_{g,R}$, four peaks are identified, labeled P_1 , P_3 , P_6 and P_8 . The magnitudes of these peaks can be analytically derived from the transmission coefficient given in Eq. (4), and they are determined by their associated probability weights C_1 , C_3 , C_6 and C_8 . In contrast, $V_{g,L} \neq V_{g,R}$, the peaks are labeled P_2 , P_4 , P_5 and P_7 , corresponding to different channels with probability weights C_2 , C_4 , C_5 and C_7 in Eq. (4). The results in Fig. 2(b) indicate that the charge transfer process corresponds to a single charge delocalization, as experimentally reported in Ref. [46].

Additionally, references [10-14] observed interesting tunneling current rectification even under small applied biases. Consequently, we present the charge stability diagram and tunneling current at the reversed bias $V_{Bias} = -1$ mV in Figs. 2(c) and 2(d). Due to the small applied bias V_{Bias} , distinguishing the stability diagram in Fig. 2(c) from that in Fig. 2(a) poses a challenge. However, notable differences in the peaks labeled P_2 and P_4 in Fig. 2(d) compared to those in Fig. 2(b) are evident. These differences in magnitude reflect the direction-dependent probabilities of tunneling current through the channels associated with C_2 and C_4 , aligning well with the observations in references [10-14].

Next, we investigate the effect of temperature on the tunneling current for both symmetrical $V_{g,L} = V_{g,R} = V_g$ and asymmetrical $V_{g,R} \neq V_{g,L}$ scenarios. In Figs. 3(a) and 3(b), we present the tunneling currents as functions of V_g and temperature T at forward and reversed biases, respectively. In Figs. 3(c) and 3(d), for the asymmetrical scenario, we show the tunneling current as a function of $V_{g,R}$ and temperature T with a fixed $e V_{g,L} = \frac{|4U_1 - U_0|}{3}$, also at forward and reversed biases. As illustrated in Figs. 3(a) and 3(b), the thermal broadening of the tunneling currents decreases with increasing temperature. This Coulomb oscillatory behavior has been reported both experimentally and theoretically in Ref. [3]. In the symmetrical case, the charge transport behavior resembles that of a single quantum dot with multiple energy levels, and the current spectra are independent of the di-

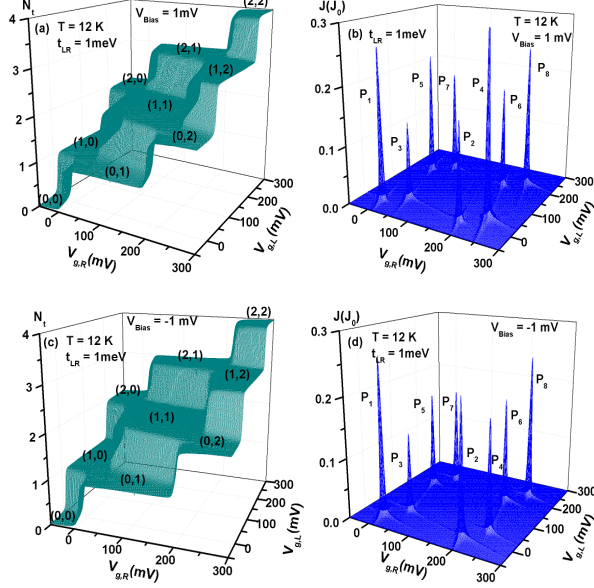


FIG. 2: (a) Total occupation number (N_t) and (b) tunneling current ($J = J_L$) as functions of gate voltages $V_{g,L}$ and $V_{g,R}$ at a temperature of $T = 12$ K and a small applied bias of $V_{Bias} = 1$ mV. (c) Total occupation number N_t and (d) tunneling current $J = |J_R|$ are calculated in the reversed bias $V_{Bias} = -1$ mV and the same temperature of $T = 12$ K. The analysis considers a AGNR heterojunction with $U_0 = 150$ meV, $U_1 = 40$ meV and $\Gamma_L = \Gamma_R = \Gamma_t = 1$ meV. For simplicity, we set $E_F = 0$, $\delta_1 = \delta_2 = 0.8$ through out this article. The tunneling currents are expressed in units of $J_0 = 0.773$ nA.

rection of the applied bias V_{Bias} . Conversely, Figs. 3(c) and 3(d) reveal the presence of nonthermal broadening in the tunneling currents. Here, the width of each tunneling current peak exhibits a temperature-independent characteristic at high temperatures, although its magnitude decays rapidly with increasing temperature. The width of each peak can be approximated as $2\sqrt{\Gamma_t^2 + t_{LR}^2}$. Notably, the tunneling current marked by P_1 in Fig. 3(d) differs from that in Fig. 3(c) at low temperatures ($k_B T < 5$ meV). We observe an increase in tunneling current with rising temperature in Fig. 3(d), which can be attributed to the lower resonant level in the reversed bias configuration. The nonthermal broadening characteristics evident in Figs. 3(c) and 3(d) indicate that the asymmetrical scenario can effectively filter thermionic charge transport arising from temperature fluctuations.

B. Tunneling Current at Large Bias

In the two-site Pauli spin blockade (PSB) configuration, we set $E_L + U_1 = E_R + U_0 = E_F = 0$ at $V_{bias} = 0$. This condition can be achieved by tuning the gate voltages to $eV_{g,L} = |4U_1 - U_0|/3$ and $eV_{g,R} = |4U_0 - U_1|/3$

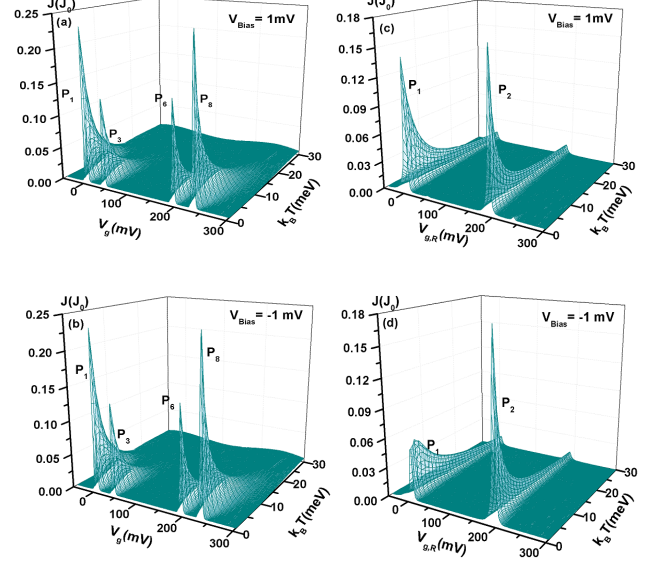


FIG. 3: Tunneling current as functions of $V_{g,L} = V_{g,R} = V_g$ and T . (a) $V_{Bias} = 1$ mV and (b) $V_{Bias} = -1$ mV. Tunneling current as functions of $V_{g,R}$ and T at $eV_{g,L} = |4U_1 - U_0|/3$. (c) $V_{Bias} = 1$ mV and (d) $V_{Bias} = -1$ mV. Other physical parameters are consistent with those in Fig. 2.

(see P_2 in Fig. 2). To examine the charge transport of SDQDs under this PSB configuration in the nonlinear response region, we present the following quantities in Fig. 4: (a) total occupation number N_t , (b) two-site correlation function of the triplet state $\langle n_{R,\sigma} n_{L,\sigma} \rangle$, (c) two-site correlation function of the singlet state $\langle n_{R,-\sigma} n_{L,\sigma} \rangle$ and (d) tunneling current J as functions of $V_{g,R}$ and V_{Bias} at fixed $eV_{g,L} = |4U_1 - U_0|/3$, $T = 12$ K and $\eta = 0$.

As shown in Fig. 4(a), N_t is constrained within the range of $1 \leq N_t \leq 2$. At zero bias ($V_{Bias} = 0$), the values of the inter-site correlation functions for the triplet state $\langle n_{R,\sigma} n_{L,\sigma} \rangle$ (Fig. 4(b)) and the singlet state $\langle n_{R,-\sigma} n_{L,\sigma} \rangle$ (Fig. 4(c)) are difficult to distinguish. When a forward bias is applied ($V_{Bias} > 0$), the inter-site correlation function of the triplet state significantly increases to approximately 0.5 with rising V_{Bias} , while the inter-site correlation function of the singlet state experiences substantial suppression. In contrast, under reversed bias conditions ($V_{Bias} < 0$), the inter-site correlation function of the triplet state becomes negligible. Although the inter-site correlation function of the singlet state exceeds that of the triplet state, it still diminishes with increasing negative V_{Bias} due to the right site being nearly filled with two particles.

A notable rectification of the tunneling current is observed in Fig. 4(d). The suppression of forward tunneling current is attributed to the occupancy of both

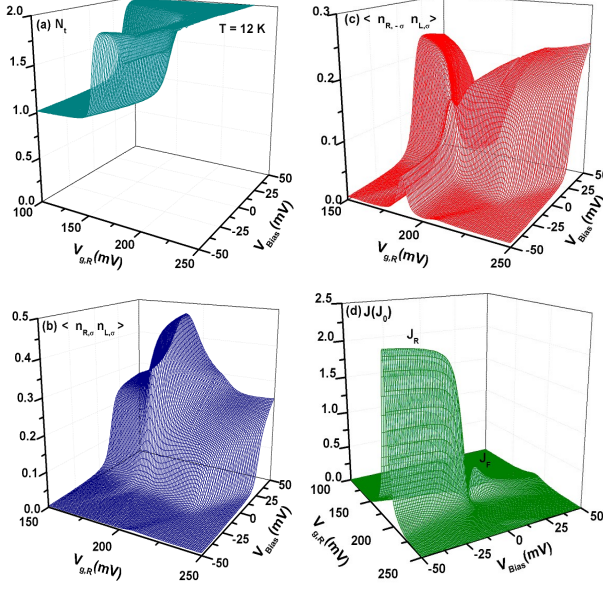


FIG. 4: (a) Total occupation number N_t , (b) inter-site correlation function of triplet states $\langle n_{R,\sigma} n_{L,\sigma} \rangle$, (c) inter-site correlation function of singlet state $\langle n_{R,-\sigma} n_{L,\sigma} \rangle$ and (d) tunneling current as function of $V_{g,R}$ and $V_{g,L}$. The gate voltage for the left site is set to $eV_{g,L} = (|4U_1 - U_0|/3)$, with $\eta = 0$ and $T = 12$ K. Other physical parameters are consistent with those used in Fig. 2.

sites by the inter-site triplet state [28–29]. Conversely, the enhancement of reversed current primarily results from the left site being unoccupied. This current rectification can be understood through the probabilities ($C_{F,PSB}$ and $C_{R,PSB}$) associated with the forward and reversed tunneling currents, given by:

$$C_{F,PSB} = N_{R,\sigma} - \langle n_{R,\sigma} n_{L,\sigma} \rangle - \langle n_{R,-\sigma} n_{R,\sigma} \rangle + \langle n_{R,-\sigma} n_{R,\sigma} n_{L,\sigma} \rangle \quad (5)$$

and

$$C_{R,PSB} = N_{R,\sigma} - \langle n_{L,\sigma} n_{R,\sigma} \rangle - \langle n_{L,-\sigma} n_{R,\sigma} \rangle + \langle n_{L,-\sigma} n_{L,\sigma} n_{R,\sigma} \rangle \quad (6)$$

For the SDQD under PSB with $1 \leq N_t \leq 2$, we find the probabilities of the J_F (J_R) as $C_{F,PSB} = \frac{1}{2} - \langle n_{R,\sigma} n_{L,\sigma} \rangle$ and $C_{R,PSB} = 1 - \langle n_{L,\sigma} n_{R,\sigma} \rangle - \langle n_{L,-\sigma} n_{R,\sigma} \rangle$. This relationship effectively explains the current rectification observed in Fig. 4.

The reversed tunneling current in Figure 4 does not exhibit the characteristic of negative differential conductance (NDC), which contrasts with experimental observations. In semiconductor SDQDs, completely avoiding bias-induced orbital offsets is challenging. To illustrate

the V_{Bias} -dependent orbital offset effect ($\eta \neq 0$) (see Appendix C), we present the tunneling current as functions of V_{Bias} and T under the PSB configuration at $\eta = 0.1$ in Figure 5. In Figure 5(a), we now observe NDC not only for forward applied bias but also for reversed bias. The orbital offset causes a shift in the resonant energy levels ($\varepsilon_L = E_L + U_1 + \eta e V_{Bias} \neq E_R + U_0 - \eta e V_{Bias} = \varepsilon_R$), leading to reduce maximum tunneling currents $J_{F,max}$ and $J_{R,max}$ compared to Figure 4(d) where $\eta = 0$. The tunneling current curves at low temperature align well with experimental measurements [10, 11].

As the temperature increases, the current rectification degrades, and the NDC behavior of the tunneling current diminishes in Figure 5(a). According to Eqs. (5) and (6), the probabilities of charge transport under the PSB configuration depend on single-particle occupation numbers and particle correlation functions. Therefore, we present the total occupation number (N_t), single-particle occupation numbers ($N_{L,\sigma}$ and $N_{R,\sigma}$), and inter-site spin correlation functions ($\langle n_{R,\sigma} n_{L,\sigma} \rangle$ and $\langle n_{R,-\sigma} n_{L,\sigma} \rangle$) of the SDQDs in Figures 5(b) through 5(f).

In Figure 5(b), the condition $1 \leq N_t \leq 2$ is maintained over a wide temperature range, indicating that the values of the three-particle correlation functions are small. As a result, $C_{F,PSB}$ and $C_{R,PSB}$ are primarily determined by the one-particle occupation number and two-particle correlation functions. The behavior of N_t shown in Figure 5(b) can be further illustrated by the occupation numbers $N_{L,\sigma}$ and $N_{R,\sigma}$ in Figures 5(c) and 5(d), respectively. Figures 5(c) and 5(d) show that, for $V_{Bias} > 0$, the two particles tend to occupy different sites, whereas for $V_{Bias} < 0$ at low temperatures ($k_B T = 1$ meV), they prefer to occupy the right site together. This explains why $C_{F,PSB} = \frac{1}{2} - \langle n_{R,\sigma} n_{L,\sigma} \rangle$ and $C_{R,PSB} = 1 - \langle n_{L,\sigma} n_{R,\sigma} \rangle - \langle n_{L,-\sigma} n_{R,\sigma} \rangle$ at low temperatures ($k_B T = 1$ meV) [30].

As the temperature increases beyond 10 meV, we see that $N_{L,\sigma}$ increases under $V_{Bias} < 0$, while $N_{R,\sigma}$ is suppressed. At high temperatures ($k_B T > 10$ meV), $N_{L,\sigma}$ and $N_{R,\sigma}$ become less sensitive to V_{Bias} . This behavior is reflected in the temperature-dependent inter-site triplet and singlet correlation functions shown in Figures 5(e) and 5(f). At high temperatures ($k_B T > 10$ meV), these two-particle correlation functions can be approximated as the product of $N_{L,\sigma}$ and $N_{R,\sigma}$. Compared to Figures 4(b) and 4(c), the orbital offset reduces the distinction between the inter-site triplet and singlet state curves. To effectively map two-electron spin states via the tunneling current with NDC, it is crucial to minimize the orbital offset effect and operate the SDQD at extremely low temperatures.

In Figure 5(a), the magnitude of tunneling currents significantly decreases with increasing temperature. To achieve stable tunneling currents across temperature variations, we consider the energy levels $\Delta_L = E_L + U_1$ and $\Delta_R = E_R + U_0$ relative to the Fermi energy ($E_F = 0$) of the electrodes. We present the reversed tunneling currents as functions of V_{Bias} and temperature T for vari-

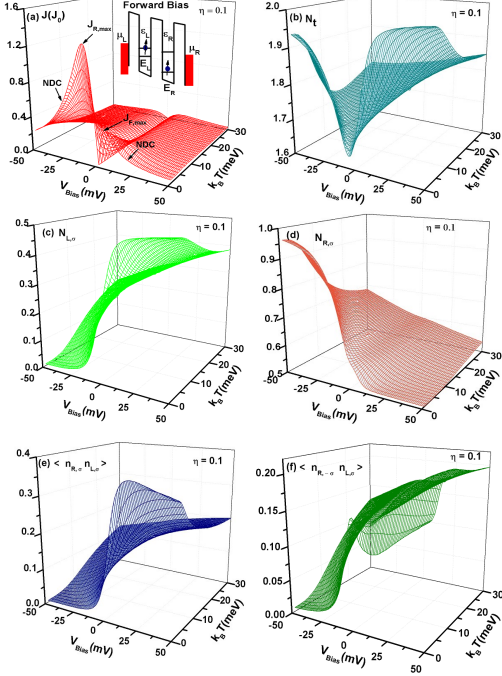


FIG. 5: (a) Tunneling current J , (b) total occupation number N_t , (c) single particle occupation number of the left site $N_{L,\sigma}$, (d) single particle occupation number of the right site $N_{R,\sigma}$, (e) inter-site triplet correlation function $\langle n_{R,\sigma}n_{L,\sigma} \rangle$, and (f) inter-site singlet correlation function $\langle n_{R,-\sigma}n_{L,\sigma} \rangle$ as functions of V_{Bias} and T . We have set $E_L = -U_1$, $E_R = -U_0$, and $\eta = 0.1$. Other physical parameters are consistent with those in Fig.2.

ous sets of Δ_L and Δ_R in Figure 6 with $\eta = 0.3$. When $\Delta_L = 50$ meV and $\Delta_R = -10$ meV, the maximum tunneling current occurs at $V_{Bias} = -100$ mV as shown in Figure 6(a), resulting from $\varepsilon_L = \Delta_L + \eta e V_{Bias} = \Delta_R - \eta e V_{Bias} = \varepsilon_R$. However, the tunneling current decays rapidly with increasing temperature. When Δ_L and Δ_R are adjusted away from E_F , the resonant channel $\varepsilon_L = \varepsilon_R$ is shifted to a larger reversed bias, resulting in a tunneling current that is less sensitive to temperature. In Figure 6(f), we observe a robust tunneling current even as the temperature rises to room temperature. This temperature-stable tunneling is attributed to the resonant channel $\varepsilon_L = \varepsilon_R = 20$ meV being coupled to the states of the electrodes under the conditions $\varepsilon_L - \mu_L \geq 2k_B T$ and $\mu_R - \varepsilon_R \geq 2k_B T$. The inset of Figure 6(f) illustrates this context, where the Fermi distribution functions indicate $f_R(\varepsilon_R) \approx 1$ and $f_L(\varepsilon_L) \approx 0$.

IV. CONCLUSION

The measurement of tunneling current through serial double quantum dots (SDQDs) remains a vibrant area of

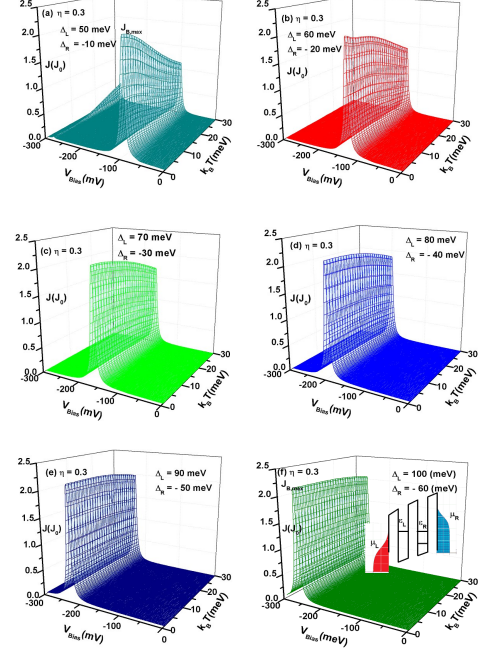


FIG. 6: Tunneling current as a function of V_{Bias} and T at $\eta = 0.3$. The energy levels $\Delta_L = E_L + U_1$ and $\Delta_R = E_R + U_0$ are introduced in the absence of applied bias. (a) $\Delta_L = 50$ meV and $\Delta_R = -10$ meV, (b) $\Delta_L = 60$ meV and $\Delta_R = -20$ meV, (c) $\Delta_L = 70$ meV and $\Delta_R = -30$ meV, (d) $\Delta_L = 80$ meV and $\Delta_R = -40$ meV, (e) $\Delta_L = 90$ meV and $\Delta_R = -50$ meV and (f) $\Delta_L = 100$ meV and $\Delta_R = -60$ meV. We have considered $\eta = 0.3$.

research, as these structures can be viewed as the smallest artificial molecules. The tunneling current spectra of SDQDs offer insights into fundamental physics and present promising applications for next-generation quantum devices. While the physical principles governing tunneling current spectra are understood, there is currently no unified formula to explain key phenomena such as coherent tunneling, Coulomb blockade, negative differential conductance (NDC), nonthermal broadening of tunneling current, and current rectification due to Pauli spin blockade.

Our study provides a closed-form expression for the tunneling current, featuring an analytic transmission coefficient that elucidates these experimental phenomena. This expression incorporates one-particle occupation numbers, two-particle inter-site correlation functions for both triplet and singlet states, as well as intra-site and three-particle correlation functions, all of which also have closed-form representations. Consequently, the tunneling current of SDQDs can be easily computed using general-purpose software such as Fortran, Python, or Mathematica. This accessibility will assist designers interested in implementing SDQD devices using various materials.

Using our closed-form tunneling current formula, we analyze the tunneling current spectra through SDQDs formed by the topological states of graphene nanoribbons. Beyond the major phenomena mentioned, we introduce a novel application of SDQDs under a Pauli spin blockade configuration, which allows for nonthermal broadening of reversed tunneling currents that remain stable across temperature variations. Transistors exhibiting temperature-independent tunneling currents with NDC can function effectively over a broad temperature range, making them crucial components in circuits for artificial intelligence applications or in extreme temperature environments.

Appendix A: Correlation functions of SDQDs

The transmission coefficient of Eq. (4) describes a particle with spin σ tunneling through serial double quantum dots (SDQDs) with energy levels E_L and E_R , modulated by gate voltages and the applied bias, respectively. Due to intra-site and inter-site Coulomb interactions, we identify eight distinct configurations with varying transport probabilities, which involve single-particle occupation numbers, two-particle correlation functions, and three-particle correlation functions[40]. The closed-form expressions for these quantities are provided below:

a: One-Particle Occupation Number

The one particle occupation number is given by $N_{\ell,\sigma} = \int \frac{d\epsilon}{\pi} G_{\ell,\sigma}^<(\epsilon)$, where the less Green's function takes following form:

$$\begin{aligned}
 G_{\ell,\sigma}^<(\epsilon) &= \Sigma_{\ell}^< \left[\frac{C_1}{|\epsilon_{\ell} - t_{\ell,j}^2/\epsilon_j|^2} + \frac{C_2}{|(\epsilon_{\ell} - U_{\ell,j}) - t_{\ell,j}^2/(\epsilon_j - U_j)|^2} \right. \\
 &+ \frac{C_3}{|(\epsilon_{\ell} - U_{\ell,j}) - t_{\ell,j}^2/(\epsilon_j - U_{j,\ell})|^2} \\
 &+ \frac{C_4}{|(\epsilon_{\ell} - 2U_{\ell,j}) - t_{\ell,j}^2/(\epsilon_j - U_j - U_{j,\ell})|^2} \\
 &+ \frac{C_5}{|(\epsilon_{\ell} - U_{\ell}) - t_{\ell,j}^2/(\epsilon_j - U_{j,\ell})|^2} \\
 &+ \frac{C_6}{|(\epsilon_{\ell} - U_{\ell} - U_{\ell,j}) - t_{\ell,j}^2/(\epsilon_j - U_j - U_{j,\ell})|^2} \\
 &+ \frac{C_7}{|(\epsilon_{\ell} - U_{\ell} - U_{\ell,j}) - t_{\ell,j}^2/(\epsilon_j - 2U_{j,\ell})|^2} \\
 &+ \left. \frac{C_8}{|(\epsilon_{\ell} - U_{\ell} - 2U_{\ell,j}) - t_{\ell,j}^2/(\epsilon_j - U_j - 2U_{j,\ell})|^2} \right] \\
 &+ t_{\ell,j}^2 \Sigma_j^< \left[\frac{C_1}{|\epsilon_{\ell}\epsilon_j - t_{\ell,j}^2|^2} + \frac{C_2}{|(\epsilon_{\ell} - U_{\ell,j})(\epsilon_j - U_j) - t_{\ell,j}^2|^2} \right. \\
 &+ \frac{C_3}{|(\epsilon_{\ell} - U_{\ell,j})(\epsilon_j - U_{j,\ell}) - t_{\ell,j}^2|^2} \\
 &+ \frac{C_4}{|(\epsilon_{\ell} - 2U_{\ell,j})(\epsilon_j - U_j - U_{j,\ell}) - t_{\ell,j}^2|^2} \\
 &+ \frac{C_5}{|(\epsilon_{\ell} - U_{\ell})(\epsilon_j - U_{j,\ell}) - t_{\ell,j}^2|^2} \\
 &+ \frac{C_6}{|(\epsilon_{\ell} - U_{\ell} - U_{\ell,j})(\epsilon_j - U_j - U_{j,\ell}) - t_{\ell,j}^2|^2} \\
 &+ \frac{C_7}{|(\epsilon_{\ell} - U_{\ell} - U_{\ell,j})(\epsilon_j - 2U_{j,\ell}) - t_{\ell,j}^2|^2} \\
 &+ \left. \frac{C_8}{|(\epsilon_{\ell} - U_{\ell} - 2U_{\ell,j})(\epsilon_j - U_j - 2U_{j,\ell}) - t_{\ell,j}^2|^2} \right]. \tag{A.1}
 \end{aligned}$$

Here, the lesser self-energies are defined as $\Sigma_{\ell}^< = \Gamma_{\ell} f_{\ell}(\epsilon)$ and $\Sigma_j^<(\epsilon) = \Gamma_j f_j(\epsilon)$, where Γ_{α} represents the tunneling rate and $f_{\alpha}(\epsilon)$ is the Fermi distribution function of the α -th electrode. For simplicity, we assume a wide-band limit for the tunneling rate and consider it to be energy-independent. The notation $\epsilon_{\ell} = \epsilon - E_{\ell} + i\Gamma_{\ell}$ is also used. The coefficients C_m denote the probability weights of each configuration in the transmission coefficient from Eq. (4). Notably, due to the absence of spin-orbit interactions and the magnetic field in the system Hamiltonian, the single-particle occupation number is spin-independent: $N_{\ell,\sigma} = N_{\ell,-\sigma}$. $N_{\ell,\sigma}$ is influenced by both electrodes.

b: Intra-site Singlet States

The two-particle correlation function for intra-site sin-

glet states is given by:

$$\begin{aligned}
& \langle n_{j,-\sigma} n_{j,\sigma} \rangle \\
&= \int \frac{d\epsilon}{\pi} (\Sigma_j^< \left[\frac{D_1}{|(\epsilon_j - U_j) - t_{\ell,j}^2/(\epsilon_\ell - U_{\ell,j})|^2} \right. \\
&+ \frac{D_2}{|(\epsilon_j - U_j - U_{\ell,j}) - t_{\ell,j}^2/(\epsilon_\ell - U_\ell - U_{\ell,j})|^2} \\
&+ \frac{D_3}{|(\epsilon_j - U_j - U_{\ell,j}) - t_{\ell,j}^2/(\epsilon_\ell - U_\ell - 2U_{\ell,j})|^2} \\
&+ \left. \frac{D_4}{|(\epsilon_j - U_j - 2U_{\ell,j}) - t_{\ell,j}^2/(\epsilon_\ell - U_\ell - 2U_{\ell,j})|^2} \right] \\
&+ t_{\ell,j}^2 \Sigma_\ell^< \left[\frac{D_1}{|(\epsilon_j - U_j)(\epsilon_\ell - U_{\ell,j}) - t_{\ell,j}^2|^2} \right. \\
&+ \frac{D_2}{|(\epsilon_j - U_j - U_{\ell,j})(\epsilon_\ell - U_\ell - U_{\ell,j}) - t_{\ell,j}^2|^2} \\
&+ \frac{D_3}{|(\epsilon_j - U_j - U_{\ell,j})(\epsilon_\ell - 2U_{\ell,j}) - t_{\ell,j}^2|^2} \\
&+ \left. \frac{D_4}{|(\epsilon_j - U_j - 2U_{\ell,j})(\epsilon_\ell - U_\ell - 2U_{\ell,j}) - t_{\ell,j}^2|^2} \right] \Big), \tag{A.2}
\end{aligned}$$

The probability weights are defined as follows: $D_1 = N_{j,\sigma} - \langle n_{j,-\sigma} n_{j,\sigma} \rangle - \langle n_{\ell,\sigma} n_{j,\sigma} \rangle + \langle n_{\ell,-\sigma} n_{\ell,\sigma} n_{j,\sigma} \rangle$, $D_2 = \langle n_{\ell,\sigma} n_{j,\sigma} \rangle - \langle n_{\ell,-\sigma} n_{\ell,\sigma} n_{j,\sigma} \rangle$, $D_3 = \langle n_{\ell,-\sigma} n_{j,\sigma} \rangle - \langle n_{\ell,-\sigma} n_{\ell,\sigma} n_{j,\sigma} \rangle$, and $D_4 = \langle n_{\ell,-\sigma} n_{\ell,\sigma} n_{j,\sigma} \rangle$. In the Pauli spin configuration, $\langle n_{j,-\sigma} n_{j,\sigma} \rangle$ is primarily influenced by the term with D_1 .

c:Inter-Site Triplet State

The two-particle correlation function for inter-site triplet states is expressed as:

$$\begin{aligned}
& \langle n_{j,\sigma} n_{\ell,\sigma} \rangle \\
&= \int \frac{d\epsilon}{\pi} (\Sigma_\ell^< \left[\frac{F_1}{|(\epsilon_\ell - U_{\ell,j}) - t_{\ell,j}^2/(\epsilon_j - U_{\ell,j})|^2} \right. \\
&+ \frac{F_2}{|(\epsilon_\ell - U_\ell - U_{\ell,j}) - t_{\ell,j}^2/(\epsilon_j - 2U_{\ell,j})|^2} \\
&+ \frac{F_3}{|(\epsilon_\ell - 2U_{\ell,j}) - t_{\ell,j}^2/(\epsilon_j - U_j - U_{\ell,j})|^2} \\
&+ \left. \frac{F_4}{|(\epsilon_\ell - U_\ell - 2U_{\ell,j}) - t_{\ell,j}^2/(\epsilon_j - U_j - 2U_{\ell,j})|^2} \right] \\
&+ t_{\ell,j}^2 \Sigma_j^< (\epsilon) \left[\frac{F_1}{|(\epsilon_\ell - U_{\ell,j})(\epsilon_j - U_{\ell,j}) - t_{\ell,j}^2|^2} \right. \\
&+ \frac{F_2}{|(\epsilon_\ell - U_\ell - U_{\ell,j})(\epsilon_j - 2U_{\ell,j}) - t_{\ell,j}^2|^2} \\
&+ \frac{F_3}{|(\epsilon_\ell - 2U_{\ell,j})(\epsilon_j - U_j - U_{\ell,j}) - t_{\ell,j}^2|^2} \\
&+ \left. \frac{F_4}{|(\epsilon_\ell - U_\ell - 2U_{\ell,j})(\epsilon_j - U_j - 2U_{\ell,j}) - t_{\ell,j}^2|^2} \right] \Big) \tag{A.3}
\end{aligned}$$

where we have $F_1 = N_{j,-\sigma} - \langle n_{j,-\sigma} n_{\ell,\sigma} \rangle - \langle n_{j,-\sigma} n_{j,\sigma} \rangle + \langle n_{j,-\sigma} n_{j,\sigma} n_{\ell,\sigma} \rangle$, $F_2 = \langle n_{j,-\sigma} n_{\ell,\sigma} \rangle - \langle n_{j,-\sigma} n_{j,\sigma} n_{\ell,\sigma} \rangle$, $F_3 = \langle n_{j,-\sigma} n_{j,\sigma} \rangle - \langle n_{j,-\sigma} n_{j,\sigma} n_{\ell,\sigma} \rangle$, and $F_4 = \langle n_{j,-\sigma} n_{j,\sigma} n_{\ell,\sigma} \rangle$.

d:Inter-Site Singlet State

The two-particle correlation function for the inter-site singlet state is expressed as:

$$\begin{aligned}
& \langle n_{j,-\sigma} n_{\ell,\sigma} \rangle \\
&= \int \frac{d\epsilon}{\pi} (\Sigma_\ell^< \left[\frac{G_1}{|(\epsilon_\ell - U_{\ell,j}) - t_{\ell,j}^2/(\epsilon_j - U_j)|^2} \right. \\
&+ \frac{G_2}{|(\epsilon_\ell - U_\ell - U_{\ell,j}) - t_{\ell,j}^2/(\epsilon_j - U_j - U_{\ell,j})|^2} \\
&+ \frac{G_3}{|(\epsilon_\ell - 2U_{\ell,j}) - t_{\ell,j}^2/(\epsilon_j - U_j - U_{\ell,j})|^2} \\
&+ \left. \frac{G_4}{|(\epsilon_\ell - U_\ell - 2U_{\ell,j}) - t_{\ell,j}^2/(\epsilon_j - U_j - 2U_{\ell,j})|^2} \right] \\
&+ t_{\ell,j}^2 \Sigma_j^< \left[\frac{G_1}{|(\epsilon_\ell - U_{\ell,j})(\epsilon_j - U_j) - t_{\ell,j}^2|^2} \right. \\
&+ \frac{G_2}{|(\epsilon_\ell - U_\ell - U_{\ell,j})(\epsilon_j - U_j - U_{\ell,j}) - t_{\ell,j}^2|^2} \\
&+ \frac{G_3}{|(\epsilon_\ell - 2U_{\ell,j})(\epsilon_j - U_j - U_{\ell,j}) - t_{\ell,j}^2|^2} \\
&+ \left. \frac{G_4}{|(\epsilon_\ell - U_\ell - 2U_{\ell,j})(\epsilon_j - U_j - 2U_{\ell,j}) - t_{\ell,j}^2|^2} \right] \Big). \tag{A.4}
\end{aligned}$$

The probability weights are defined as: $G_1 = N_{j,\sigma} - \langle n_{j,\sigma} n_{\ell,\sigma} \rangle - \langle n_{j,-\sigma} n_{j,\sigma} \rangle + \langle n_{j,-\sigma} n_{j,\sigma} n_{\ell,\sigma} \rangle$, $G_2 = \langle n_{j,\sigma} n_{\ell,\sigma} \rangle - \langle n_{j,-\sigma} n_{j,\sigma} n_{\ell,\sigma} \rangle$, $G_3 = \langle n_{j,-\sigma} n_{j,\sigma} \rangle - \langle n_{j,-\sigma} n_{j,\sigma} n_{\ell,\sigma} \rangle$, and $G_4 = \langle n_{j,-\sigma} n_{j,\sigma} n_{\ell,\sigma} \rangle$.

e:Three Particle Correlation Functions

The three-particle correlation function is given by:

$$\begin{aligned}
& \langle n_{j,-\sigma} n_{j,\sigma} n_{\ell,\sigma} \rangle \\
&= \int \frac{d\epsilon}{\pi} (\Sigma_\ell^< \left[\frac{W_1}{|(\epsilon_\ell - 2U_{\ell,j}) - t_{\ell,j}^2/(\epsilon_j - U_j - U_{\ell,j})|^2} \right. \\
&+ \frac{W_2}{|(\epsilon_\ell - U_\ell - 2U_{\ell,j}) - t_{\ell,j}^2/(\epsilon_j - U_j - 2U_{\ell,j})|^2} \\
&+ t_{\ell,j}^2 \Sigma_j^< \left[\frac{W_1}{|(\epsilon_\ell - 2U_{\ell,j})(\epsilon_j - U_j - U_{\ell,j}) - t_{\ell,j}^2|^2} \right. \\
&+ \left. \frac{W_2}{|(\epsilon_\ell - U_\ell - 2U_{\ell,j})(\epsilon_j - U_j - 2U_{\ell,j}) - t_{\ell,j}^2|^2} \right] \Big). \tag{A.5}
\end{aligned}$$

The probability weights are defined as: $W_1 = \langle n_{j,-\sigma} n_{j,\sigma} \rangle - \langle n_{j,-\sigma} n_{j,\sigma} n_{\ell,\sigma} \rangle$, and $W_2 = \langle n_{j,-\sigma} n_{j,\sigma} n_{\ell,\sigma} \rangle$. Using Eqs. (A.1) to (A.5), we solve these correlation functions self-consistently. Once we obtain the solutions, we substitute them back into the transmission coefficient from Eq. (4) to calculate the tunneling current of the SDQDs as described in Eq. (3).

Appendix B: Charge stability diagram and electrical conductance for the case of $t_{LR} > \Gamma_t$

In Fig. 2, we present the charge stability diagrams and tunneling current under small applied biases ($V_{Bias} = \pm 1$ mV) for the condition $t_{LR} = \Gamma_t = 1$ meV, where distinguishing between sequential tunneling and coherent tunneling is challenging. To better understand the coherent tunneling process, we consider the condition

$t_{LR} > \Gamma_t$. In Fig. B.1, we show the charge stability diagram (N_t) and electrical conductance (G_e) as functions of two gate voltages ($V_{g,L}$ and $V_{g,R}$) at $\Gamma_t = 1$ meV and $T = 12$ K, using the contour color-fill presentation.

Diagrams (a) and (b) in Fig. B.1 display the calculated values of N_t and G_e at $t_{LR} = 1$ meV, while diagrams (c) and (d) show the same quantities for $t_{LR} = 5$ meV. Diagrams (a) and (b) in Fig. B.1 can be directly compared with diagrams (a) and (b) in Fig. 2. In Fig. B.1(a), the region marked as (1,1) exhibits a honeycomb shape, which is consistent with the findings in ref [33]. Additionally, the particle number transition zones are clearly visible between the different plateaus. In Fig. B.1(b), we observe eight small spots corresponding to eight configurations for the case of $t_{LR} = \Gamma_t$. As shown in this panel, charge transport occurs only at the particle number transition zones. When $t_{LR} > \Gamma_t$ (coherent tunneling regime), the region marked as (1,1) in the charge stability diagram undergoes a modification[41]. In particular, the particle number transition zones change significantly, as illustrated in Fig. B.1(c). The electrical conductance exhibits butterfly-like shapes in Fig. B.1(d). In the symmetric case ($V_{g,L} = V_{g,R}$), each butterfly wing is symmetrical. In the asymmetric case ($V_{g,L} \neq V_{g,R}$), the wings of each butterfly become asymmetrical.

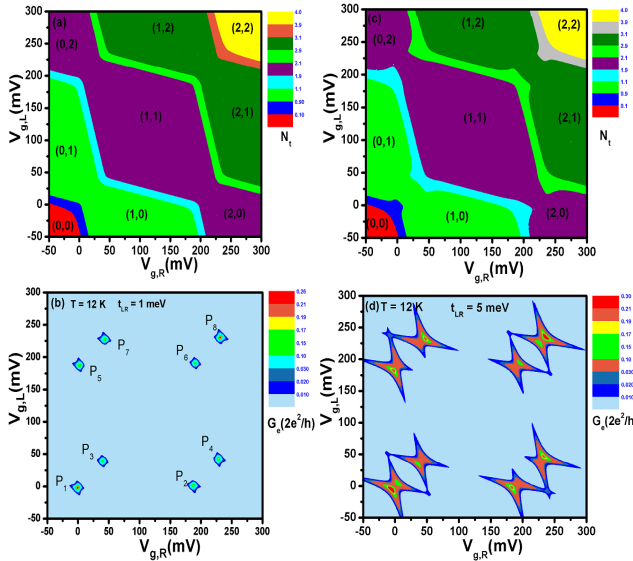


FIG. B.1: (a) Total occupation number (N_t) and (b) electrical conductance (G_e) as functions of gate voltages $V_{g,L}$ and $V_{g,R}$ at a temperature of $T = 12$ K and $t_{LR} = \Gamma_t = 1$ meV. (c) Total occupation number (N_t) and (d) electrical conductance (G_e) calculated for $t_{LR} = 5$ meV, with the same temperature of $T = 12$ K and $\Gamma_t = 1$ meV. All other physical parameters are the same as those of Fig. 2. The electrical conductance is expressed in units of $G_0 = \frac{2e^2}{h}$.

Appendix C: Stark shift of the topological states in a 9-7-9 AGNR structure under an electric field

To illustrate the Stark shift of the interface states in $9_w - 7_x - 9_y$ AGNR structures under a uniform electric field[47,48], where w , x , and y represent the number of unit cells in the AGNRs, we plot the energy levels as functions of the applied bias V_{Bias} for various x values in Fig. C. 1, with $w = y = 8$. In Fig. C. 1(a), notations E_c and E_v denote the energy levels for the conduction and valence subband edge states, respectively. Symbols Σ_L and Σ_R represent the left and right zigzag edge states of $9_8 - 7_5 - 9_8$ AGNR structure, while $E_{I,L}$ and $E_{I,R}$ correspond to the energy levels of the interface states of the AGNR heterojunctions.

At zero applied bias, Σ_L and Σ_R nearly merge due to the very weak coupling between the left and right zigzag edge states. In contrast, $E_{I,L}$ and $E_{I,R}$ are separated by $|2t_{LR}|$, where the electron hopping strength $t_{LR} = 37.7$ meV arising from the strong coupling between the left and right interface states. The charge density for the interface states of the $9_8 - 7_5 - 9_8$ AGNR structures is shown in Fig. 1(b). The results in Fig. C. 1(a) indicate that while the subband states (E_c and E_v) exhibit a red Stark shift, the topological states (Σ_L , Σ_R , $E_{I,L}$ and $E_{I,R}$) show a blue Stark shift. When V_{Bias} is smaller than 0.5V, $E_{I,L}$ and $E_{I,R}$ remain well separated from the subband states. As x increases from 5 to 10, t_{LR} becomes very small, resulting in $E_{I,L} = -E_{I,R} = t_{LR} \approx 2.5$ meV for $x = 10$. Additionally, the parameter $\eta \approx 0.215$ can be determined based on the behavior of $E_{I,L(R)}$ as functions of V_{Bias} . The results in Fig. C. 1 demonstrate that t_{LR} and η can be engineered by varying the configurations of 9-atom and 7-atom AGNR segments. Finally, it is worth noting that the topological states Σ_L and Σ_R do not exist in the transmission spectra of 9-7-9 AGNR with zigzag edges coupled to electrodes. This highlights that the interface states serve as the only channels for electron tunneling through the topological states of 9-7-9 AGNR structures.

Data Availability

The data that supports the findings of this study are available within the article.

Conflicts of interest

There are no conflicts to declare.

Acknowledgments

This work was supported by the National Science and Technology Council, Taiwan under Contract No. MOST 107-2112-M-008-023MY2.

E-mail address: mtkuo@ee.ncu.edu.tw

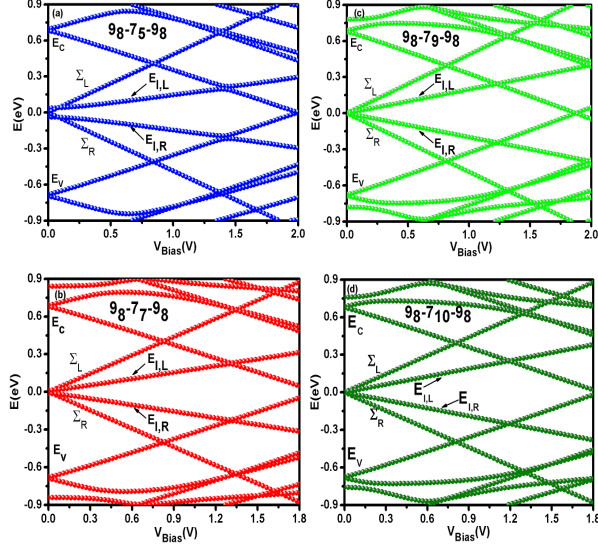


FIG. C.1: Energy levels of 9-7-9 AGNR structure as functions of the applied bias V_{Bias} for various 7-atom AGNR segment lengths: (a) $9_8 - 7_5 - 9_8$, (b) $9_8 - 7_7 - 9_8$, (c) $9_8 - 7_9 - 9_8$, and (d) $9_8 - 7_{10} - 9_8$.

-
- ¹ P. W. Anderson, Phys. Rev. **109**, 1492 (1958).
 - ² P. A. Lee and T. V. Ramakrishnan, Rev. Mod. Phys. **57**, 287 (1985).
 - ³ Y. Meir, N. S. Wingreen, and Patrick A. Lee, Phys. Rev. Lett. **66**, 3048 (1991).
 - ⁴ V. Madhavan, W. Chen, T. Jamneala, M. F. Crommie, N. S. Wingreen, Science **280**, 567 (1998).
 - ⁵ D. Goldhaber-Gordon, H. Shtrikman, D. Mahalu, D. Abusch-Magder, U. Meirav, M. A. Kastner, Nature **391**, 156 (1998).
 - ⁶ D. Goldhaber-Gordon, J. Gores, M. A. Kastner, Hadas Shtrikman, D. Mahalu, and U. Meirav, Phys. Rev. Lett. **81**, 5225 (1998).
 - ⁷ F. R. Waugh, M. J. Berry, D.J. Mar, R. M. Westervelt, K. L. Campman and A. C. Gossard, Phys. Rev. Lett. **75**, 705 (1995).
 - ⁸ J. R. Petta, A. C. Johnson, C. M. Marcus, M. P. Hanson, and A. C. Gossard, Phys. Rev. Lett. **93**, 186802 (2004).
 - ⁹ W. G. van der Wiel, S. De Franceschi, J. M. Elzerman, T. Fujisawa, S. Tarucha, L. P. Kouwenhoven, REVIEWS OF MODERN PHYSICS, **75**, (2003).
 - ¹⁰ K. Ono, D. G. Austing, Y. Tokura, and S. Tarucha, Science **297**, 1313 (2002).
 - ¹¹ A. C. Johnson, J. R. Petta, C. M. Marcus, M. P. Hanson, and A. C. Gossard, Phys. Rev. B **72**, 165308 (2005).
 - ¹² M. G. Borselli, K. Eng, E. T. Croke, B. M. Maune, B. Huang, R. S. Ross, A. A. Kiselev, P. W. Deelman, I. Alvarado-Rodriguez, A. E. Schmitz, M. Sokolich, K. S. Holabird, T. M. Hazard, M. F. Gyure, A. T. Hunter, Appl. Phys. Lett. **99**, 063109 (2011).
 - ¹³ N. S. Lai, W. H. Lim, C. H. Yang, F. A. Zwanenburg, W. A. Coish, F. Qassemi, A. Morello and A. S. Dzura, SCIENTIFIC REPORTS **1**, 110 (2011).
 - ¹⁴ R. Y. Li, F. E. Hudson, A. S. Dzura, and A. R. Hamilton, Nano Letters, **15**, 7314 (2015).
 - ¹⁵ C. Tong, A. Kurzman, R. Garreis, W. W. Huang, S. Jele, M. Eich, Lev Ginzburg, C. Mittag, K. Watanabe, T. Taniguchi, K. Ensslin, and T. Ihn, Phys. Rev. Lett. **128**, 067702 (2022).
 - ¹⁶ He Liu, Ting Zhang, Ke Wang, Fei Gao, Gang Xu, Xin Zhang, Shu-Xiao Li, Gang Cao, Ting Wang, Jianjun Zhang, Xuedong Hu, Hai-Ou Li, and Guo-Ping Guo, Phys. Rev. Appl. **17**, 044052 (2022).
 - ¹⁷ N. W. Hendrickx, L. Massai, M. Mergenthaler, F. J. Schupp, S. Paredes, S. W. Bedell, G. Salis and A. Fuhrer, Nature Materials **23**, 920 (2024).
 - ¹⁸ D. P. DiVincenzo, Science, **309**, 2173 (2005).
 - ¹⁹ T. Fujisawa, T. Hayashi, R. Tomita and Y. Hirayama, Science **312**, 1634 (2006).
 - ²⁰ R. Hanson and D. D. Awschalom, Nature, **453**, 1043 (2008).
 - ²¹ C. C. Chen and Y. C. Chang, Phys. Rev. B **92**, 245406 (2015).
 - ²² M. Golor, C. Koop, T. C. Lang, S. Wessel, and M. J.

- Schmidt, Phys. Rev. Lett. **111**, 085504 (2013).
- ²³ Y. C. Chen, T. Cao, C. Chen, Z. Pedramraz, D. Haberer, D. G. de Oteyza, R. Fischer, S. G. Louie and M. F. Crommie, Nature. Nanotechnol. **10**, 156 (2015).
 - ²⁴ D. J. Rizzo, G. Veber, J. W. Jiang, R. McCurdy, T. Bronner, T. Cao, T. Chen, S. G. Louie, F. R. Fischer and M. F. Crommie, Science, **369**, 1597 (2020).
 - ²⁵ D. J. Rizzo, J. W. Jiang, D. Joshi, G. Veber, C. Bronner, R. A. Durr, P. H. Jacobse, T. Cao, A. Kalayjian, H. Rodriguez, P. Butler, T. Chen, S. G. Louie, F. R. Fischer and M. F. Crommie, ACS Nano, **15**, 20633 (2021).
 - ²⁶ M. J. J. Mangnus, F.R. Fischer, M. F. Crommie, I. Swart, and P.H. Jacobse, Phys. Rev. B **105**, 115424 (2022).
 - ²⁷ F. Borsoi, N. W. Hendrickx, V. John, M. Meyer, S. Motz, F. van Riggelen, A. Sammak, Sander L. de Snoo, G. Scappucci and M. Veldhorst, Nature nanotech **19**, 21 (2024).
 - ²⁸ J. Fransson and M. Rasander, Phys. Rev. B **73**, 205333 (2006).
 - ²⁹ J. Inarrea, G. Platero and A. H. MacDonald, Phys. Rev B **76**, 085329 (2007).
 - ³⁰ M. R. Buitelaar, J. Fransson, A. L. Cantone, C. G. Smith, D. Anderson, G. A. C. Jones, A. Ardavan, A. N. Khlobystov, A. A. R. Watt, K. Porfyrakis, and G. A. D. Briggs, Phys. Rev. B **77**, 245439 (2008).
 - ³¹ J. Danon and Y. V. Nazarov, Phys. Rev. B **80** 041301(R) (2009).
 - ³² A. Palyi and G. Burkard, Phys. Rev. B **80** 201404 (R) (2009).
 - ³³ D. Das Sarma, X. Wang, and S. Yang, Phys. Rev. B **83**, 235314 (2011).
 - ³⁴ X. Wang, S. Yang, and S. Das Sarma, Phys. Rev. B **84**, 115301 (2011).
 - ³⁵ David M. T. Kuo, S. Y. Shiau, and Y. C. Chang, Phys. Rev. B **84**, 245303 (2011).
 - ³⁶ W. J. Hou, Y. D Wang, J. H. Wei and Y. J. Yan, J. Chem. Phys, **146**, 224304 (2017).
 - ³⁷ M. Kondo, S. Miyota, W. Izumida, S. Amaha and T. Hatano, Phys. Rev. B **103** 155414 (2021).
 - ³⁸ David M. T. Kuo, Nanotechnolog, **34**, 505401 (2023).
 - ³⁹ H. Haug and A. P. Jauho, Quantum Kinetics in Transport and Optics of Semiconductors (Springer, Heidelberg, 1996).
 - ⁴⁰ David M. T. Kuo, C. C. Chen, and Y. C. Chang, Phys. Rev. B **95**, 075432 (2017).
 - ⁴¹ F. Molitor, S. Droscher, J. Guttinger, A. Jacobsen, C. Stampfer, T. Ihn, and K. Ensslin, Appl. Phys. Lett. **94**, 222107 (2009).
 - ⁴² S. Moriyama, Daiju Tsuya, Eiichiro Watanabe, S. Uji, M. Shimizu, T. Mori, T. Yamaguchi, and K. Ishibashi, Nano Lett. **9**, 2891 (2009).
 - ⁴³ X. L. Liu, Dorothee Hug, and Lieven M. K. Vandersypen, Nano Lett. **10**, 1623 (2010).
 - ⁴⁴ L. Banszerus, B. Frohn, A. Epping, D. Neumaier, K. Watanabe, T. Taniguchi, and C. Stampfer, Nano Lett. **18**, 4785 (2018).
 - ⁴⁵ L. Banszerus, S. Moller, E. Icking, Kenji Watanabe, T. Taniguchi, C. Volk, and C. Stampfer, Nano Lett. **20**, 2005 (2020).
 - ⁴⁶ T. Hatano, M. Stopa, and S. Tarucha, Science **309**, 268 (2005).
 - ⁴⁷ David M T Kuo, Journal of Physics: Condensed Matter, **37**, 085304 (2025).
 - ⁴⁸ David M T Kuo, RSC Adv., **14**, 20113 (2024).